Very long wave infrared quantum cascade detector based on modular band structure

Kai Guo (郭 凯)[1,2,3], Yu Chen (陈 雨)[2,3], Yixuan Zhu (朱怡璇)[2,3], Kun Li (黎 昆)[2,3], Shenqiang Zhai (翟慎强)[2], Fengqi Liu (刘峰奇)[2,3], Jilong Tang (唐吉龙)[1], Xiaohua Wang (王晓华)[1]*, Zhipeng Wei (魏志鹏)[1], and Junqi Liu (刘俊岐)[2,3]*****

[1]*State Key Laboratory of High Power Semiconductor Lasers, School of Physics, Changchun University of Science and Technology, Changchun 130022, China*

[2]*Key Laboratory of Semiconductor Materials Science, Institute of Semiconductors, Chinese Academy of Sciences, Beijing 100083, China*

[3]*Center of Materials Science and Opto-Electronic Technology, University of Chinese Academy of Sciences, Beijing 101408, China*

Corresponding author: biewang2001@126.com; ** corresponding author: zpweicust@126.com; * corresponding author: jqliu@semi.ac.cn*

Received Month X, XXXX; accepted Month X, XXXX; posted online Month X, XXXX

The optoelectronic performance of quantum cascade detectors (QCDs) is highly sensitive to the design of the energy level structure, leading to the inability of a single structure to achieve broad wavelength tuning. To address this issue, we propose and demonstrate a modular concept for very long wave infrared (VLWIR) QCDs based on a miniband diagonal transition scheme. The modular design makes the wavelength tuning only need to be adjusted for the absorption quantum well module rather than for the whole active region. Theoretical simulation shows that the wavelength tuning range is 39.6meV (~ 14-30 μm). To prove the feasibility of the scheme, three samples with different absorption well widths were fabricated and characterized. At 10 K, the response wavelengths of the three QCDs are 14, 16, and 18 μm, respectively, corresponding to responsivities and detectivities exceeding 2 mA/W and 1×10^{10} Jones.

Keywords: Quantum cascade detector; Very long wave infrared; Modular band structure; Miniband diagonal transition; Wide tuning range.

DOI: 10.3788/COLXXXXXX.XXXXXX.

1. Introduction

Quantum cascade detectors (QCDs), a new type of photovoltaic quantum well infrared photodetector (QWIP), have been presented and gained great progresses over the past decades[1,2]. Typically, the wells and the barriers of QCDs are composed of two different semiconductor materials, such as GaAs/AlGaAs, InGaAs/InAlAs, and InGaAs/AlAsSb. Besides, based on bound-to-bound intersubband (ISB) transitions in a built-in asymmetric conduction band structure, QCDs exhibit the characteristics of tailorable operation wavelength, low noise photovoltaic mode, and room temperature operation, which are advantageous over well-established detectors[3,4]. Meanwhile, as an unipolar photodetector, the sub-picosecond electron ISB scattering time makes QCD have a very high frequency response, thereby providing them with application potential in fields such as free-space optical communication and on-chip sensing[5-7].

So far, QCDs are able to cover a wide spectral range from the near- to far-infrared spectral region[8-14]. In the very long wave infrared (VLWIR) region (λ~14-30 μm), QCDs have attracted special attentions for their potential applications in astronomical observation, atmospheric monitoring and intrusion detection fields[15]et al. Many quantum designs for VLWIR QCDs have been proposed[13,16-18] to decrease the dark current noise and improve the responsivity, such as the energy mini-steps[17] and twin-well absorption region[16]. Certain improvement in the device performance was demonstrated, but these structures are mainly narrow band designs resulting in an optimized structure targeting only one specific wavelength. Therefore, a highly robust quantum bandstructure which is insensitive to wavelength tuning is urgently needed for VLWIR QCDs.

In this letter, a modular miniband diagonal transition (MDT) bandstructure strategy is proposed for VLWIR QCDs. This structure enables the QCDs to tune the wavelength in a modular manner. The theoretical simulation shows that the response wavelength of QCDs with different well width can cover the range of 14-29.5 μm, while maintaining high extraction efficiency (>90%) and dipole matrix element (DME >1.38 nm). Three devices with different well widths were fabricated with the center wavelengths of 14, 16, and 18 μm respectively. At 10 K, the detectivities of all three samples exceeded 1×10^{10} Jones, with corresponding responsivities of 7 mA/W, 11 mA/W, and 2.5 mA/W, respectively. The experimental results are in good agreement with the numerical simulations, which proves the capability of the modular design based on the MDT scheme for wide wavelength tuning in VLWIR.

2. Structural design and Simulation

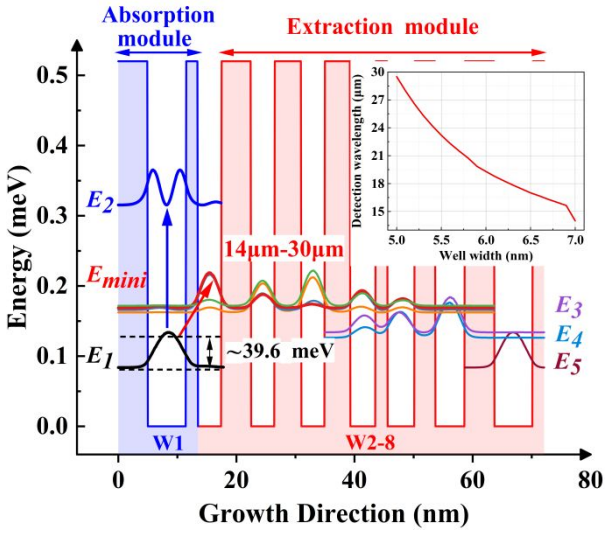

Fig. 1. Modular conduction band structure of VLWIR QCD. The entire structure is based on the $In_{0.53}Ga_{0.47}As/In_{0.52}Al_{0.48}As$ material system. The thicknesses of the layers in one stage are W1(**7.0**), 2, **3.95**, 5, **4**, 4.5, **4**, 4.3, **4.3**, 1.95, **4.6**, 3.5, **5**, and 5 nm, where the underlined values correspond to absorption transition well (W1) and the bold numbers correspond to the $In_{0.53}Ga_{0.47}As$ layer. Inset: Detection wavelength as a function of the W1 well width.

In order to obtain a VLWIR QCD band structure that is insensitive to wide tuning, two aspects must be considered. First, the band structure should be modular, so that wavelength tuning can be achieved by adjusting for specific modules rather than for the whole active region. Second, the proposed quantum bandstructure can effectively address the inherent issues of electron thermal backfill and non-radiative diagonal transition in VLWIR QCD. In response to these points, a miniband diagonal transition (MDT) structure is proposed, as shown in Fig. 1. The diagonal transition enables optical transitions between two adjacent wells, which overcomes the electron extraction scheme based on resonant tunneling (which requires stringent energy level alignment), thus realizing the modular design of band structures. The band structure consists of absorption (blue) and extraction (red) modules, and by matching different functional modules, the device can achieve the control of parameters such as wavelength, electron transport, resistance, dark current, etc. In addition, the smaller wavefunction overlap of the diagonal transition also helps to improved thermal backfilling of the upper level electrons. In the extraction module, the miniband is utilized as the upper level to enhance electron extraction efficiency, while the increased spatial gap between the ground state and the step levels effectively suppresses the non-radiative transition process. Furthermore, the miniband consists of four levels with a band width of 10.1 meV, this effectively broadens the response bandwidth accordingly.

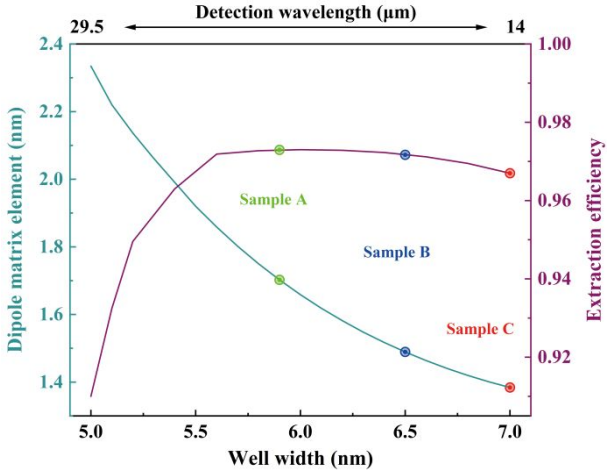

Fig. 2. Dipole matrix element (DME) and extraction efficiency of devices at various well width (W1). The green, blue, and red marker points correspond to the three experimental samples with different well widths below.

The entire tuning process is realized by changing the width of the W1 well in the absorption module. As the width of W1 well decreases, the E_1 level will gradually rise, and the corresponding transition energy between E_1 and E_{mini} will gradually decrease, resulting in a longer response wavelength. The tuning range of the E_1 level is about 39.6 meV, which is approximately one LO-phonon energy. The inset in Fig. 1 shows the detection wavelengths at different W1 well widths. When the well width is varied in the range of 5-7 nm, the response wavelength covers the range of 14-29.5 μm. In addition, to investigate the effect of MDT structure on the performance of devices for different response wavelengths, the extraction efficiency and dipole matrix element (DME) were calculated as shown in Fig. 2. As the well width increases, the extraction efficiency exhibits a trend of initially increasing and then decreasing, but the minimum value still exceeds 90%. This weak wavelength dependence of the extraction efficiency proves the high robustness of the MDT structure. The DME is another important parameter reflecting the QCD performance, and its squared value is proportional to the ISB absorption strength. As seen

in Fig. 2, the DME is positively correlated with the response wavelength, with values of 1.38 nm and 2.3 nm at 14 μm and 29.5 μm, respectively. It is worth noting that the DME at 14 μm wavelength is already close to 1.42 nm for the $E_1 - E_2$ vertical transition and much higher than 0.98 nm[11] for the bound-to-bound diagonal transitions.

Under illumination, the electrons in the ground state E_1 absorb photons and a diagonal transition to the miniband is excited. After the transportation in the miniband, two energy steps separated by the E_3 and E_4 levels are passed through by longitudinal optical (LO) phonon scattering to reach the ground state E_5 of the next period, and finally are collected by the external circuit. For different detection wavelengths, since they have the same extraction module, the corresponding extraction efficiency and DME are essentially the same. Therefore, device performance is mainly affected by two transition processes, namely E_1-E_{mini} and $E_{3/4}$-E_5. When the detection wavelength increases, the energy gaps for both E_1-E_{mini} and $E_{3/4}$-E_5 decrease. At this point, electrons on the E_1 level are more likely to be affected by thermal noise during the diagonal transition process, leading to certain electron losses. Similarly, the electron transport efficiency from the $E_{3/4}$ level to the E_5 level also decreases because the energy gap between them no longer satisfies a LO-phonon energy. Moreover, the probability of thermal escape of electrons on the E_5 level to the E_3/E_4 level also increases.

3. Sample fabrication

To verify the capability of widely tailorable wavelength coverage of the MDT structure, three samples with the same material structure except for different absorption transition well (W1) widths in the active region, corresponding to 7.0 nm, 6.5 nm, and 5.9 nm, were grown and fabricated. The active region is based on lattice matched $In_{0.53}Ga_{0.47}As/In_{0.52}Al_{0.48}As$ materials. The layer information (composition and thickness) of one cascade period can be found in the caption of Fig. 1. The QCD wafers were grown on a semi-insulating InP substrate by metal-organic chemical vapor deposition (MOCVD) system equipped with a close-coupled showerhead growth chamber. During the growth process, the growth chamber was maintained at a low-pressure environment of 100 mbar. For the designed structure, the growth temperature and rate of the active region were controlled at 600 °C and ~0.2 nm/s, respectively. All samples were composed of the active region with 30 repetitions are inserted between the upper (200 nm) and lower (500 nm) contact layers. The doping concentrations of Si in the absorption well (W1) and the contact layers are 1×10^{17} cm^{-3} and 2×10^{18} cm^{-3}, respectively.

The material quality and internal structure of the samples were investigated by high resolution X-ray diffraction (XRD). Figure 3 presents the XRD rocking curves of the three samples. Clearly, the satellite peaks of all samples are very narrow (15-20 arcsec), indicating that they possess good periodicity and low interface roughness. According to the position of the satellite peak, the periodic thickness of the three samples were obtained as 58.852, 59.408, and 60.203 nm, respectively, within 1.86% thicker than the nominal design values. Nevertheless, the variation in the periodic thickness among samples due to the different widths of the W1 wells corresponds well with the measured values.

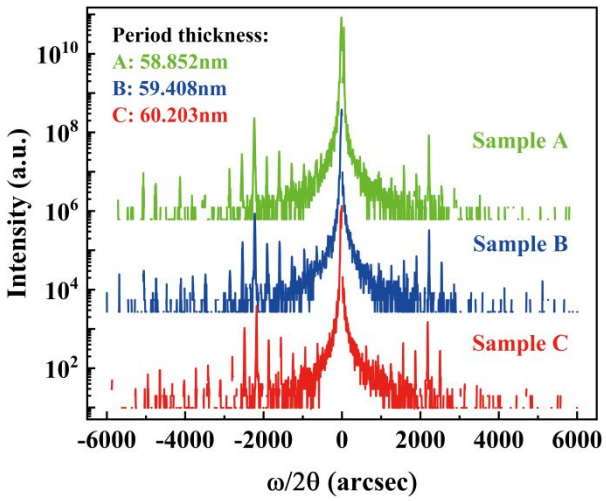

Fig.3. X-ray diffraction (XRD) rocking curves of three QCD samples.

Finally, the wafer was processed into 200×200 μm^2 mesas using standard lithography and wet etching processes. A 450-nm-thick SiO_2 sidewall passivation layer was then deposited using plasma-enhanced chemical vapor deposition. Ohmic contacts were fabricated by the deposition of Ti/Au on the top and bottom contact layers. To perform photocurrent measurements, the facets of the sample were polished into 45° to meet the QW selection rules requirement for TM polarized excitation.

4. Results and Discussion

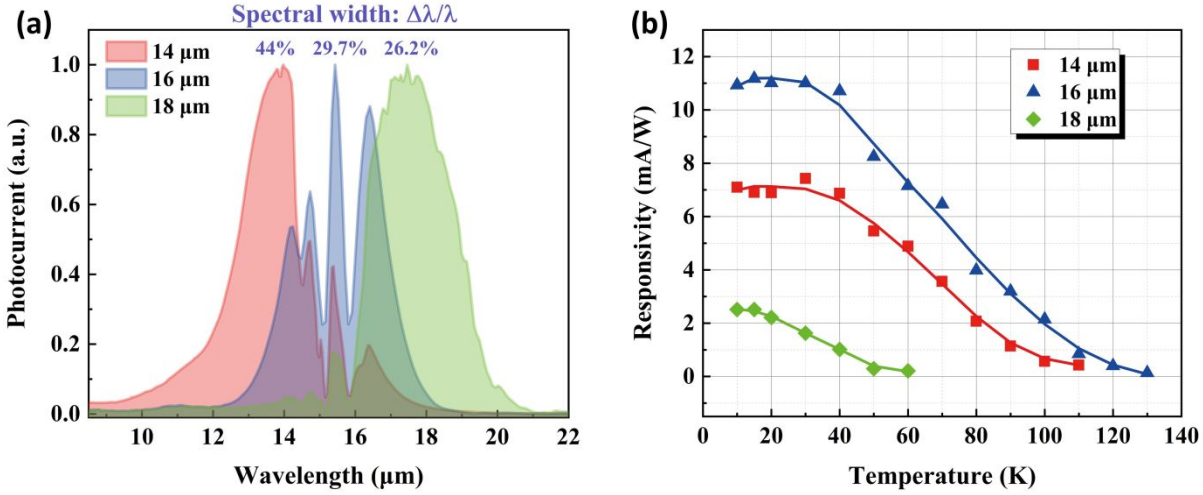

Fig.4. (a) The normalized photocurrent spectra of three samples at 10 K, and (b) their peak responsivity at different temperatures.

Optical measurements of the QCD were performed using a Bruker Vertex 70v Fourier-transform infrared spectrometer and a thermal source. Light is irradiated onto QCD from a 45 ° InP substrate. Figure 4(a) shows the normalized photocurrent spectra of three samples at 10 K. It is evident that effective light detection can still be achieved by simply changing the width of well W1. The peak wavelengths of the three samples, corresponding to 14, 16, and 18 μm, are in well agreement with the theoretical calculations in the inset of Fig. 1. The three distinct dips are attributed to the absorption by CO_2 (667 cm^{-1}) and InP two-phonon (632 and 660 cm^{-1}). These dips can be mitigated separately by using a vacuum spectrometer and a substrate thinning scheme. In addition, the influence of miniband as an upper level on spectral width has also been observed. Here, the spectral width is defined as the ratio of the wavelength difference (Δλ) of 10% above the baseline to the peak wavelength (λ). At 10 K, the spectral widths of all three samples exceeded 26%, with a maximum width of 44% for 14 μm. This result is 6.3 times wider than the bound-to-bound design (7%)[11], and also exceeds the broadband QCD (27.3%) based on the multi-core active region (26 differently designed active region) structure [19]. It is worth noting that the total spectral width of the three samples exceeded 10 μm, which represents a new design concept for broadband QCDs.

Using the photoresponse spectra and the blackbody photocurrent, the responsivity of the samples can be obtained as shown in Fig. 4(b). The responsivity of all devices shows a trend of initially increasing and then decreasing with increasing temperature, which can be explained by the inefficient ionization of the donor dopants at low temperatures[11]. Among the three samples, the 14 μm and 16 μm QCD have similar performance, with responsivities of 7 mA/W and 11 mA/W at 10 K, respectively, and corresponding operating temperatures reaching 110 K and 130 K. Compared with the other two samples, the device performance of 18 μm QCD showed a slight degradation. The responsivity is 2.5 mA/W at 10 K and the maximum operating temperature is 60 K. It is worth noting that this result better than the reported QCDs at an identical wavelength[17].

The product of the area of the device (A) and its R_0 at 0 V bias is indicative of the Johnson noise in the detector. Based on the results of dark current-voltage (not shown here), the differential resistance-area products (R_0A) are plotted as functions of temperature for the three devices, as depicted in Fig. 5(a). At low temperatures (<40 K), R_0A demonstrates non-linearity. This is because the dark current noise of the device gradually changes from thermal noise to photon noise as the dominant factor. Due to the fact that photon noise does not depend on device temperature, R_0A tends to be a constant within this temperature range. Through linear fitting, the thermal activation energies of the three samples can be derived, which are 47.5 meV (14 μm), 45.4 meV (16 μm), and 60.6 meV (18 μm), respectively. Reflected in the conduction band diagram, these values primarily correspond to the energy between the E_1 and E_3 / E_4 levels. The four resonantly coupled wells forming the miniband increase the spatial separation of the two levels, which will effectively suppress the diagonal electronic leakage and thus improve the noise characteristics of the device.

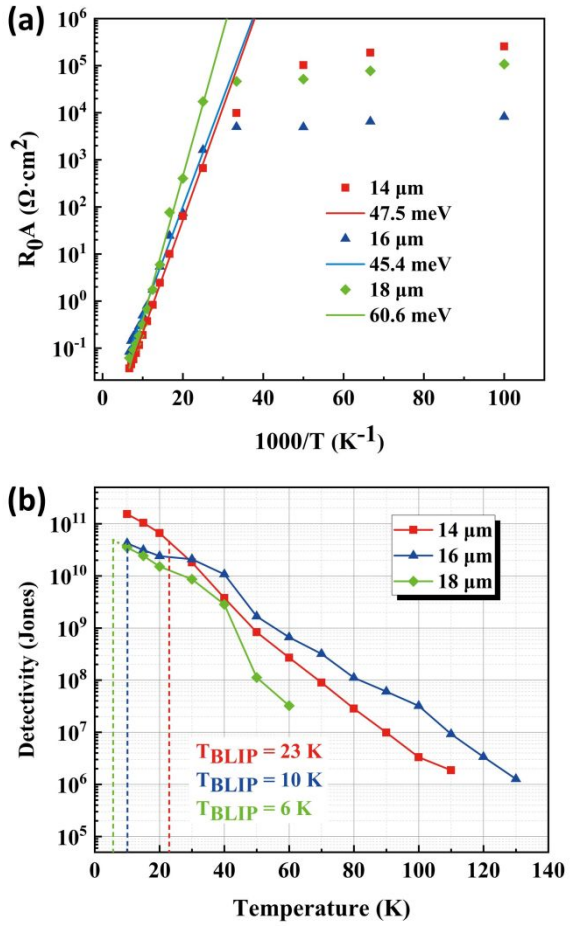

Fig. 5. (a) The differential resistance-area product R_0A and (b) detectivity of three samples as functions of temperature.

From the peak responsivity, R_0A, the Johnson noise limited detectivity ($D_J^* = R_P\sqrt{R_0A/4K_BT}$) for QCDs is estimated[20]. Figure 5(b) shows the D_J^* of the three devices along with the calculated background limited detectivities (D_{BLIP}^*). At 10 K, the D_J^* of 14, 16, and 18 μm QCDs are 1.53×10^{11}, 4.2×10^{10}, and 3.5×10^{10} Jones, respectively. These results are better than the previous VLWIR QCDs with a detectivity of 2.2×10^{9} Jones at 10 K[18]. The D_{BLIP}^* corresponds to the value at which the detectivity no longer changes when the temperature drops to a critical temperature, and this critical temperature is the background limited temperature (T_{BLIP}). The D_{BLIP}^* for 14, 16, and 18 μm QCDs are 4.63×10^{10}, 4.7×10^{10}, and 4.84×10^{10} Jones, respectively, showing an upward trend with increasing wavelength. Their corresponding T_{BLIP} are 23, 10, and 6 K respectively. Within this temperature range, the device maintains a good temperature stability.

5. Conclusion

In this work, we propose a modular band structure for VLWIR QCD to achieve wide wavelength tuning. The miniband diagonal transition design realizes this modular structure and provides high extraction efficiency and absorption strength. In theory, a wide spectral coverage (~ 14-30 μm) can be achieved by independently adjusting the absorption module. Finally, three samples with different well widths were designed and fabricated to verify the feasibility of the proposed scheme. At 10 K, the response wavelengths of the three devices are 14, 16, and 18 μm, respectively. Among them, the 16 μm QCD shows the best performance, with a peak responsivity of 11 mA/W, a D_J^* of 1.53×10^{11} Jones and a maximum operating temperature of 130 K.

Acknowledgement

This work was supported by the National Natural Science Foundation of China (Nos. 61835011, 62335015, 12393830, 62222408, 12274404), the Key Program of the Chinese Academy of Sciences (Nos. XDB43000000), and the Youth Innovation Promotion Association of the Chinese Academy of Sciences (Nos. 2022112).

References

1. L. Gendron, M. Carras, A. Huynh, V. Ortiz, C. Koeniguer, and V. Berger, "Quantum cascade photodetector", Appl. Phys. Lett. **85**, 2824 (2004).
2. T. Dougakiuchi, A. Ito, M. Hitaka, K. Fujita, and M. Yamanishi, "Ultimate response time in mid-infrared high-speed low-noise quantum cascade detectors", Appl. Phys. Lett. **118**, 041101 (2021).
3. F. R. Giorgetta, E. Baumann, M. Graf, Q. Yang, C. Manz, K. Kohler, H. E. Beere, D. A. Ritchie, E. Linfield, A. G. Davies, Y. Fedoryshyn, H. Jackel, M. Fischer, J. Faist, and D. Hofstetter, "Quantum Cascade Detectors", IEEE J. Quantum Electron. **45**, 1039 (2009).
4. L. Wang, S. Zhai, F. Wang, J. Liu, S. Liu, N. Zhuo, C. Zhang, L. Wang, F. Liu, and Z. Wang, "A Polarization-Dependent Normal Incident Quantum Cascade Detector Enhanced Via Metamaterial Resonators", Nanoscale Res. Lett. **11**, 536 (2016).
5. T. Dougakiuchi, A. Ito, M. Hitaka, K. Fujita, and M. Yamanishi, "Ultimate response time in mid-infrared high-speed low-noise quantum cascade detectors," Appl. Phys. Lett. 118, 041101 (2021).
6. P. Didier, H. Dely, T. Bonazzi, O. Spitz, E. Awwad, É. Rodriguez, A. Vasanelli, C. Sirtori, and F. Grillot, "High-capacity free-space optical link in the midinfrared thermal

atmospheric windows using unipolar quantum devices," Adv. Photonics 4, 056004 (2022).

7. B. Schwarz, P. Reininger, D. Ristanić, H. Detz, A. M. Andrews, W. Schrenk, and G. Strasser, "Monolithically integrated mid-infrared lab-on-a-chip using plasmonics and quantum cascade structures," Nat. Commun. 5, 4085 (2014).
8. A. Vardi, G. Bahir, F. Guillot, C. Bougerol, E. Monroy, S. E. Schacham, M. Tchernycheva, and F. H. Julien, " Near infrared quantum cascade detector in GaN/AlGaN/AlN heterostructures", Appl. Phys. Lett. **92**, 011112 (2008).
9. F. R. Giorgetta, E. Baumann, D. Hofstetter, C. Manz, Q. Yang, K. Köhler, and M. Graf, "InGaAs/AlAsSb quantum cascade detectors operating in the near infrared", Appl. Phys. Lett. **91**, 111115 (2007).
10. M. Graf, N. Hoyler, M. Giovannini, J. Faist, and D. Hofstetter, "InP-based quantum cascade detectors in the mid-infrared", Appl. Phys. Lett. **88**, 241118 (2006).
11. K. Li, F. Ren, S. Liu, J. Liu, N. Zhuo, Y. Zhu, S. Zhai, J. Zhang, L. Wang, Y. Li, and F. Liu, "High responsivity quantum cascade detectors with bound-to-miniband diagonal transition", Appl. Phys. Lett. **119**, 051101 (2021).
12. K. Li, S. Liu, N. Zhuo, J. Liu, Y. Zhu, K. Guo, S. Zhai, J. Zhang, L. Wang, Y. Li, and F. Liu, "Quantum cascade detectors with enhanced responsivity using coupled double-well structures", Appl. Phys. Express **15**, 032005 (2022).
13. A. Buffaz, M. Carras, L. Doyennette, A. Nedelcu, X. Marcadet, and V. Berger, "Quantum cascade detectors for very long wave infrared detection", Appl. Phys. Lett. **96**, 172101 (2010).
14. M. Graf, G. Scalari, D. Hofstetter, J. Faist, H. Beere, E. Linfield, D. Ritchie, and G. Davies, "Terahertz range quantum well infrared photodetector", Appl. Phys. Lett. **84**, 475 (2004).
15. Y. Chen, B. Wang, Y. Zang, C. Zhang, H. Zhang, Y. Yuan, D. Zhou, L. Hou, M. Pan, and X. Wang, "The High-Performance Imaging Verification of Si:P Blocked Impurity Band Detector for Very-Long-Wave-Infrared Spectral Range", IEEE J. Quantum Electron. 56, 4000506 (2020).
16. K. Guo, Y. Zhu, K. Li, J. Liu, S. Zhai, S. Liu, N. Zhuo, J. Zhang, L. Wang, F. Liu, X. Wang, and Z. Wei, "Very long wave infrared quantum cascade detector with a twin-well absorption region", Appl. Phys. Lett. **121**, 061101 (2022).
17. S. Zhai, J. Liu, X. Wang, N. Zhuo, F. Liu, Z. Wang, X. Liu, N. Li, and W. Lu, "19 μm quantum cascade infrared photodetectors", Appl. Phys. Lett. **102**, 191120 (2013).
18. F. R. Giorgetta, E. Baumann, M. Graf, L. Ajili, N. Hoyler, M. Giovannini, J. Faist, D. Hofstetter, P. Krötz, and G. Sonnabend, " 16.5 μm quantum cascade detector using miniband transport", Appl. Phys. Lett. **90**, 231111 (2007).
19. D. Hofstetter, F. R. Giorgetta, E. Baumann, Q. Yang, C. Manz, and K. Köhler, "Midinfrared quantum cascade detector with a spectrally broad response", Appl. Phys. Lett. **93**, 221106 (2008).
20. M. Giparakis, H. Knötig, H. Detz, M. Beiser, W. Schrenk, B. Schwarz, G. Strasser, and A. M. Andrews, " 2.7 μm quantum cascade detector: Above band gap energy intersubband detection", Appl. Phys. Lett. **120**, 071104 (2022).